

Impact of the Test Device on Acoustic Emission Signals from Nuclear Safety Experiments: Contribution of Wave Propagation Modeling to Signal Processing

Traore Oumar Issiaka, Favretto-Cristini Nathalie, Cristini Paul, Pantera Laurent and Viguiet-Pla Sylvie

Abstract—A strongly energetic spectral component has been observed in the operating noise of a research reactor before the beginning of reactivity initiated accidents (RIA). We identify the source of this component by means of analytical derivations of torsional wave propagation in the test device. Numerical simulations, performed with a spectral-element method, confirm that this component is a resonant frequency of the device, and allow to evaluate the impact of wave travel path in the test device on the acoustic emission signals recorded during RIA experiments. The transfer function of the test device is strongly dependent on both the source and the receiver locations, which precludes signal processing by deconvolution when the location of the AE source mechanism is unknown. Moreover, the geometry and the configuration of the test device may not influence signals in the low-frequency range, and hence the signals generated by source mechanisms located on the fuel clad such as clad failures. Finally, replacing the heat transfer fluid (pressurized water) by sodium leads to an increase in the recorded signal amplitude and a small shift of the frequency content towards the high frequencies. The results obtained in this paper may be useful to improve design of future RIA experiments. They are also useful to understand wave propagation in the core of the reactor and to choose appropriate signal processing tools for recovering the source of acoustic emission signals generated during RIA experiments.

Index Terms—Acoustic Emission, Reactivity Initiated Accident, Wave Propagation, Spectral Element Modeling

I. INTRODUCTION

Reactivity Initiated Accident (RIA) is a nuclear reactor accident which involves an unexpected and very fast increase in fission rate and reactor power due to the ejection of a control rod. The power increase may damage the fuel clad and the fuel pellets of the reactor. The French Alternative Energies and Atomic Energy Commission (CEA) operates a pool-type reactor dedicated to fuel behavior study in RIA conditions. Several non-destructive methods, including the acoustic emission (AE) technique, are used to inspect the reactor and to get information on the behavior of the fuel clad

Oumar Issiaka Traore, Nathalie Favretto-Cristini and Paul Cristini are with Aix-Marseille Univ., CNRS, Centrale Marseille, LMA, France (Email: toumarissiaka@gmail.com, favretto@lma.cnrs-mrs.fr, cristini@lma.cnrs-mrs.fr)

Laurent Pantera is with CEA, DEN, DER/SRES, Cadarache, F13108 Saint-Paul-Lez-Durance, France (Email: laurent.pantera@cea.fr)

Sylvie Viguiet-Pla is with Université de Perpignan via Domitia, LAMPS, 52 av. Paul Alduy, 66860 Perpignan Cedex 9, France and Université Paul Sabatier, 118 Route de Narbonne, F-31062 Toulouse Cedex 9, France (Email: viguiet@math.univ-toulouse.fr)

and the fuel pellets during the experiments. The AE technique is a powerful tool dedicated to structure health monitoring which has also the advantage of being simple to adapt to nuclear-oriented purposes. It is generally used to monitor real-time processes which emit acoustic waves. In nuclear industry, it has thus been used mainly to monitor the pressure vessels and the primary circuit [1]–[3]. More recently, it has been used to monitor the compaction of nuclear fuel powders [4], [5] as well.

Whatever the non-destructive testing method, one of the trickiest tasks is the effective interpretation and exploitation of the received information. This is even more important for AE testing. The received information is composed of numerous transient signals resulting from wave propagation generated by unknown source mechanisms one seeks to identify. It is potentially corrupted by several parameters among which the choice and the settings of the AE acquisition system [6], the environmental noise and the wave propagation path in the structure. From a mathematical point of view, if the environmental noise n is assumed to be additive, the received AE signal x can be expressed as:

$$x(t) = h_1 * h_2 * s(t) + n(t), \quad t \in \{1, \dots, N\} \quad (1)$$

where $*$ denotes the convolution operator, h_1 and h_2 correspond to the impact of the structure and the acquisition system, respectively, s is the signal associated with the physical source mechanism of interest and t the time. One of the key problems of a AE testing process is the estimation of the source signal s . The functions h_1 , h_2 and n have to be studied in order to be properly removed from the recorded signal x .

The environment of industrial reactors is very noisy and the potential sources of n are numerous. Furthermore, in the case of research reactors fluctuations in the noise level and/or its stochastic behavior are usually observed, which has a great impact on the recorded signals. However, whatever the noise level and behavior, more or less sophisticated methods are found to be efficient for structural change detection and acoustic signal denoising [7], [8]. In general, the transfer function h_2 is obtained from the calibration tests of the acquisition system and deconvolution is then

sufficient to remove its potential impact on x [9]. On the contrary, evaluating the transfer function h_1 is quite tricky, since it depends on the location of both the source and the receiver and on the physical and geometrical properties of the structure. Nevertheless, in the case of RIA experiments this evaluation may be valuable, since analysis of the operating noise of the reactor put light on the occurrence of a strongly energetic spectral component around the frequency 180 kHz for almost all the fourteen experiments carried out at CEA up to now (Figure 1). As it was recorded before the power increase representative of a RIA, it cannot be attributed to a physical mechanism. However, this component, still present during the whole experiment, is energetic enough to hide valuable information about the potential source mechanisms of interest here. As a consequence, if we want to efficiently characterize these mechanisms, it is crucial to identify the source of this spectral component, in order to avoid its occurrence during the next planned experiments and/or use appropriate signal processing to remove it. Knowing that this component is not generated by the AE acquisition system, Equation (1) suggests that its potential source is either the environmental noise n , or the impact h_1 of wave propagation inside the test device. The purpose of the work presented in this paper is then to identify this source by evaluating h_1 .

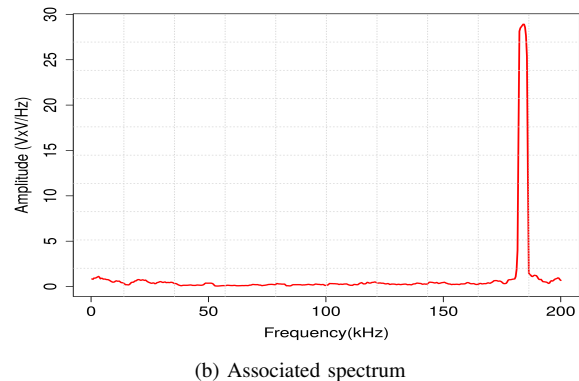
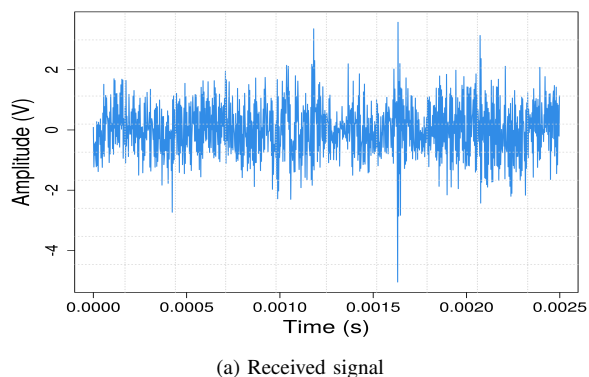


Figure 1: Example of operating noise recorded by AE sensor before the beginning of RIA experiments carried out in 1997

Usually, the transfer function h_1 is evaluated using experimental, analytical or numerical approaches. The

experimental approach, which consists in studying the wave propagation following various paths in the structure through active acoustical measurements, cannot be applied here. Indeed, due to the hostile environment and the complex geometry of the test device, together with the needs for controlling both the source and the receivers, it is tricky to perform numerous realistic measurements in order to correctly evaluate h_1 . When the structure geometry can be simplified and reduced to a simple configuration which can be solved, the analytical approach is useful, for instance, to determine the resonant frequencies of the structure. For more complex structures, the numerical approach is a valuable alternative tool for understanding wave propagation [10] and, possibly, the impact of changes in the acquisition design of experiments.

In this paper, we propose to rely on both analytical and numerical approaches, in order to understand wave propagation in the test device used for RIA experiments. The objective of our work is twofold. We want to determine the resonant frequencies of the test device, in order to potentially link them to the spectral component (180 kHz) previously observed during experiments. We also want to evaluate the impact of the location of both the source and the receiver on the transfer function h_1 . In addition, the impact of a change in the heat transfer fluid (sodium or pressurized water) on the AE signals is also studied. The obtained results might be useful, for instance, to improve design of future RIA experiments.

The paper is then organized as follows. In Section 2 we briefly present the test device of RIA experiments. From acoustical considerations we simplify the geometrical and physical properties in order to get an equivalent device more suitable for the analytical derivations and the numerical simulations of wave propagation presented in the subsequent sections. In Section 3 the resonant frequency of the simplified test device is obtained through the frequency equation and for the specific case of torsional modes. Section 4 focuses on numerical simulations of wave propagation in the test device, based on a spectral-element method. The impact of changes in the experiment conditions on the transfer function h_1 is investigated. Finally, obtained results are discussed in Section 5.

II. DESCRIPTION AND SIMPLIFICATION OF THE TEST DEVICE

The RIA experiments are performed in an open pool-type research reactor composed of a driver core made of a thousand of UO_2 rods and specially designed to support an injection of reactivity. The reactor includes an experimental loop specially designed to receive, in the center of the driver core, the instrumented test device housing the fuel rod to be tested (Figure 2). The test device is equipped with several sensors (including two piezoelectric AE sensors) to control the experiment and to characterize the behavior of the fuel rod during the power burst. The AE sensors are made of lithium niobate cristal with a pass-band of $5 - 400\text{ kHz}$ and a resonant frequency of 25 kHz . They are designed to work in nuclear harsh environment up to 600 degrees Celsius. They are located at the top and the bottom of the fuel rod,

respectively, and are distant of 2 m (Figure 2). A (40 dB) preamplifier is associated with each sensor. The sampling rate is $2.5 \mu s$.

In the following, we focus only on a part of the test device of 3 m long which includes the sensors and the fuel rod. This choice is suitable for studying the wave propagation, since it takes into account all the possible locations of the source mechanisms of interest. In this zone, the device can be considered as a (more or less) cylindrical stratified medium with different types of fine (fluid or solid) layers of few millimeters, from the fuel rod of UO_2 to the outer layer of Zircaloy (Figure 3). The presence of a thin layer of Xenon, which is a gas with a much lower impedance than that of the surrounding materials (Table I), allows us to greatly simplify the test device characteristics. Indeed, considering an incident wave travelling from the device core towards the outer layers, the impedance contrast between the Zircaloy and the Xenon layers implies a quasi-null wave transmission beyond the Zircaloy layer, and therefore a wave propagation confined in a four-layered medium (Figure 4).

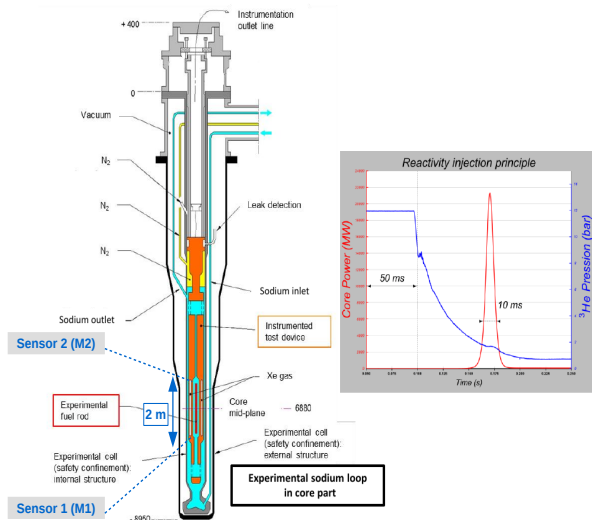


Figure 2: Sketch of the RIA research reactor and the test device containing the fuel sample.

Our approach, combining analytical derivations and numerical simulations, implies to consider two models with different levels of complexity. The first one, represented in Figure 4a, corresponds to a simplified test device, of length 3m and diameter 17.2mm, which accounts for only the simplification relative to the Xenon barrier. This model is considered for the numerical simulations. The second model, considered for the analytical derivations and illustrated in Figure 4b, corresponds to a simplified test device of the same size as the previous one, but now composed of only three materials (namely, Uranium, Zircaloy and Sodium). Indeed, due to the frequencies and wavelengths involved here (namely, around $200kHz$ and a couple of centimeters, respectively), the presence of the Zircaloy fuel clad can be neglected, since its

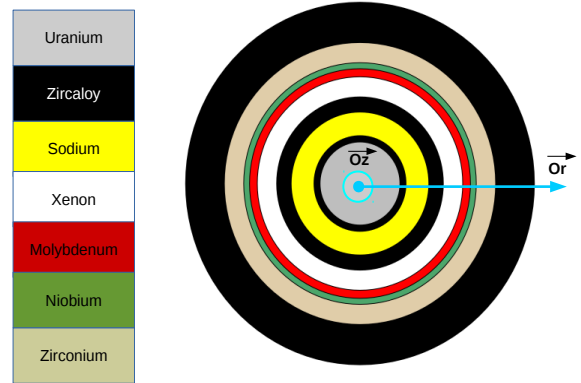


Figure 3: Radial section of the test device at $(z = 0, \theta = 0)$ illustrating the different types of media involved. Note that the scale of the illustration is not real although representative.

Table I: Physical properties (densities, P- and S-wave velocities, and associated impedances) of the different media involved in the test device (cf Figure 3)

| Material | ρ (kg/m^3) | c_P (m/s) | c_S (m/s) | Z_P | Z_S |
|-----------------|------------------------|--------------------|--------------------|-------------------|-------------------|
| Uranium | 11000 | 3370 | 2020 | $3,70 \cdot 10^7$ | $2,22 \cdot 10^7$ |
| Zircaloy | 6500 | 4720 | 2360 | $3,07 \cdot 10^7$ | $1,53 \cdot 10^7$ |
| Stainless steel | 7900 | 5460 | 3070 | $4,31 \cdot 10^7$ | $2,42 \cdot 10^7$ |
| Sodium | 968 | 2300 | - | $2,23 \cdot 10^6$ | - |
| Water | 1000 | 1436 | - | $1,44 \cdot 10^6$ | - |
| Xenon | 6 | 1090 | - | 6540 | - |
| Molybdenum | 10190 | 6679 | 3525 | $6,81 \cdot 10^7$ | $3,59 \cdot 10^7$ |
| Niobium | 8400 | 5068 | 2092 | $4,26 \cdot 10^7$ | $1,76 \cdot 10^7$ |
| Zirconium | 6400 | 4650 | 2300 | $2,98 \cdot 10^7$ | $1,47 \cdot 10^7$ |

thickness ($0.625mm$) is much smaller than that of the Uranium layer ($4.125mm$). Moreover, since the transmission coefficient at the Uranium/Stainless steel interface tends to unity, the Stainless steel layer located at the bottom of the test device can be replaced by an Uranium layer. All these simplifications greatly facilitate the subsequent analytical derivations.

III. ANALYTICAL STUDY OF WAVE PROPAGATION INSIDE THE SIMPLIFIED TEST DEVICE

The length/width ratio of the test device being about 174, we can consider here that the simplified test device, represented in Figure 4b, can be approximated by an infinitely long three-layered cylinder of diameter 17.2mm which includes a semi-infinite (along the Oz axis) rigid core of Uranium. Wave propagation within cylindrical media is widely reported in the literature. Here, we rely on well-known results in order to analyze the specific case related to the test device. The reader can refer, for instance, to [11]–[13] for further details.

Consider that the displacement vector \vec{u} is expressed as the sum of a vector potential $\vec{\psi}$ and a scalar potential ϕ :

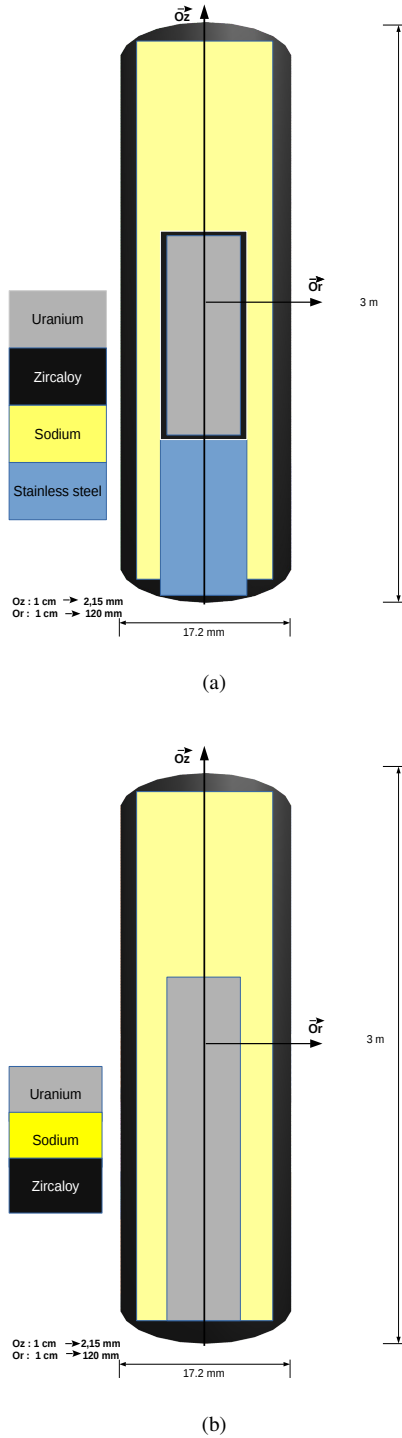


Figure 4: Longitudinal section of the simplified test device, of length $3m$ and diameter $17.2mm$, considered for the numerical simulations (a) and the analytical derivations (b).

$$\vec{u} = \vec{grad} \phi + \vec{rot} \cdot \vec{\psi} \quad (2)$$

both satisfying the wave equation

$$-\frac{1}{c^2} \frac{\partial^2 \xi}{\partial t^2} + \Delta \xi = 0 \quad (3)$$

where c is the velocity of the bulk P - or S -waves associated with the scalar and vector potentials, respectively. Solving Eq.(3) in the cylindrical coordinate system by using the method of separation of variables leads to the following general expressions for the scalar potential ϕ and for the components ψ_r , ψ_θ , and ψ_z of the vector potential $\vec{\psi}$:

$$\begin{aligned} \phi(r, \theta, z; t) &= \phi_r(r) \cos(n\theta) e^{i(kz-\omega t)} \\ \psi_r(r, \theta, z; t) &= \psi_{rr}(r) \cos(n\theta) e^{i(kz-\omega t)} \\ \psi_\theta(r, \theta, z; t) &= \psi_{\theta r}(r) \sin(n\theta) e^{i(kz-\omega t)} \\ \psi_z(r, \theta, z; t) &= \psi_{zr}(r) \cos(n\theta) e^{i(kz-\omega t)} \end{aligned} \quad (4)$$

where θ and ω are the angular coordinate and the angular frequency, respectively. We have:

$$\begin{aligned} \phi_r &= A_1 Z_n(\alpha r) + A_2 W_n(\alpha r) \\ \psi_{zr} &= D_1 Z_n(\beta r) + D_2 W_n(\beta r) \\ \psi_{rr} &= B_1 Z_{(n+1)}(\beta r) + B_2 W_{(n+1)}(\beta r) \\ \psi_{\theta r} &= -\psi_{rr} \end{aligned} \quad (5)$$

where $k = \omega/c$ is the wavenumber related to the propagation mode, $\alpha^2 = k^2 - k_p^2$ and $\beta^2 = k^2 - k_s^2$, the indexes p and s referring to the P - and S -waves propagating in the solid medium. Moreover, A_1 , A_2 , B_1 , B_2 , D_1 and D_2 are unknown constants, and Z_n and W_n are the Bessel functions (of order n) of the first and second kind, respectively. Expression (2) then allows us to obtain the components of the displacement vector \vec{u} as a function of those of the scalar and vector potentials:

$$\begin{aligned} u_r &= \left(\frac{\partial \phi_r}{\partial r} + \frac{n}{r} \psi_{zr} + i k \psi_{rr} \right) \cos(n\theta) e^{i(kz-\omega t)} \\ u_\theta &= \left(-\frac{n}{r} \phi_r + i k \psi_{rr} - \frac{\partial \psi_{zr}}{\partial r} \right) \sin(n\theta) e^{i(kz-\omega t)} \\ u_z &= \left(i k \phi_r - \frac{\partial \psi_{rr}}{\partial r} - \frac{n+1}{r} \psi_{rr} \right) \cos(n\theta) e^{i(kz-\omega t)} \end{aligned} \quad (6)$$

A. Frequency equation

Since the simplified test device has been likened to a cylinder with a semi-infinite (along the Oz axis) rigid core, we have [14], [15]:

$$\psi_r(r, \theta, z; t) = \psi_\theta(r, \theta, z; t) = 0 \quad (7)$$

Thus, expression (6) of the components of the displacement vector \vec{u} becomes:

$$\begin{aligned} u_r &= \left(\frac{\partial \phi_r}{\partial r} + \frac{n}{r} \psi_{zr} \right) \cos(n\theta) e^{i(kz-\omega t)} \\ u_\theta &= \left(-\frac{n}{r} \phi_r - \frac{\partial \psi_{zr}}{\partial r} \right) \sin(n\theta) e^{i(kz-\omega t)} \\ u_z &= i k \phi_r \cos(n\theta) e^{i(kz-\omega t)} \end{aligned} \quad (8)$$

Since the origin of the Oz axis is in the Uranium core, the Bessel functions associated with the solution to the Bessel differential equation in this medium are reduced to those of the first kind. By denoting by 1 the index of this medium, and by combining expressions (5) and (8), we then get:

$$\begin{aligned} u_r^1 &= \left[A_{11} \alpha_1 Z_n'(\alpha_1 r) + \frac{n}{r} D_{11} Z_n(\beta_1 r) \right] \cos(n\theta) e^{i(k_1 z - \omega t)} \\ u_\theta^1 &= \left[-\frac{n}{r} A_{11} Z_n(\alpha_1 r) - D_{11} \beta_1 Z_n'(\beta_1 r) \right] \sin(n\theta) e^{i(k_1 z - \omega t)} \\ u_z^1 &= i k_1 A_{11} Z_n(\alpha_1 r) \cos(n\theta) e^{i(k_1 z - \omega t)} \end{aligned} \quad (9)$$

where $Z_n' = \frac{\partial Z_n}{\partial r}$.

Assuming that the heat transfer fluid (here, Sodium) is a perfect fluid, and denoting by 2 the index of this medium, only P -waves can propagate and the displacement is linked to the scalar potential ϕ_2 through :

$$u_r^2 = g \vec{rad} \phi_2, \quad (10)$$

with

$$\phi_2 = [E_{21} Z_n(\alpha_2 r) + E_{22} W_n(\alpha_2 r)] \cos(n\theta) e^{i(k_2 z - \omega t)} \quad (11)$$

where E_{21} and E_{22} are unknown constants.

Finally, by denoting by 3 the index of the outer layer (Zircaloy), and by combining expressions (5) and (8), we get :

$$\begin{aligned} u_r^3 &= \left[A_{31} \alpha_3 Z_n'(\alpha_3 r) + A_{32} \alpha_3 W_n'(\alpha_3 r) \right. \\ &\quad \left. + \frac{n}{r} D_{31} Z_n(\beta_3 r) + \frac{n}{r} D_{32} W_n(\beta_3 r) \right] \cos(n\theta) e^{i(k_3 z - \omega t)} \\ u_\theta^3 &= \left[-\frac{n}{r} A_{31} Z_n(\alpha_3 r) - \frac{n}{r} A_{32} W_n(\alpha_3 r) \right. \\ &\quad \left. - D_{31} \beta_3 Z_n'(\beta_3 r) - D_{32} \beta_3 W_n'(\beta_3 r) \right] \sin(n\theta) e^{i(k_3 z - \omega t)} \\ u_z^3 &= [i k_3 A_{31} Z_n(\alpha_3 r) + i k_3 A_{32} W_n(\alpha_3 r)] \cos(n\theta) e^{i(k_3 z - \omega t)} \end{aligned} \quad (12)$$

Applying the proper boundary conditions at the Uranium/Sodium and Sodium/Zircaloy interfaces:

$$p^{fluid} = \sigma_{rr}^{solid} ; \quad u_r^{fluid} = u_r^{solid} \quad \text{and} \quad \sigma_{r\theta}^{solid} = 0 \quad (13)$$

and the free surface condition at the surface of the Zircaloy layer:

$$\sigma_{rr} = 0 \quad \text{and} \quad \sigma_{r\theta} = 0 \quad . \quad (14)$$

leads to a system of eight equations with eight unknowns (*cf* Appendix A), namely $A_{11}, D_{11}, E_{21}, E_{22}, A_{31}, A_{32}, D_{31}$ and D_{32} corresponding to the displacement amplitudes in the different media:

$$[\mathbf{M}] \vec{x} = 0 \quad (15)$$

where \mathbf{M} is a 8×8 matrix whose coefficients are given in Appendix B, and $\vec{x} = (A_{11}, D_{11}, E_{21}, E_{22}, A_{31}, A_{32}, D_{31}, D_{32})$. Setting the determinant of \mathbf{M} to zero leads to express the frequency equation associated with the simplified test device of interest here. Depending on the different values of n , the solution of this equation allows to identify the different propagation modes associated with the simplified test device, each mode having specific properties [11]–[13].

B. Particular case of torsional modes

The torsional modes correspond to the solutions to the so-called frequency equation when $n = 0$. One of the main characteristics of these modes is that the displacement vector \vec{u} then consists of a single component u_θ [12], the scalar potential ϕ and the components ψ_r and ψ_θ of the vector potential $\vec{\psi}$ being equal to zero. The matrix \mathbf{M} associated with the simplified test device is thus written as :

$$\mathbf{M} = \begin{pmatrix} a_{11} & 0 & a_{13} & a_{14} & 0 & 0 & 0 & 0 \\ a_{21} & 0 & a_{23} & a_{24} & 0 & 0 & 0 & 0 \\ 0 & a_{32} & 0 & 0 & 0 & 0 & 0 & 0 \\ 0 & 0 & a_{43} & a_{44} & a_{45} & a_{46} & a_{47} & a_{48} \\ 0 & 0 & a_{53} & a_{54} & a_{55} & a_{56} & a_{57} & a_{58} \\ 0 & 0 & 0 & 0 & a_{65} & a_{66} & a_{67} & a_{68} \\ 0 & 0 & 0 & 0 & a_{75} & a_{76} & a_{77} & a_{78} \\ 0 & 0 & 0 & 0 & a_{85} & a_{86} & a_{67} & a_{68} \end{pmatrix} \quad (16)$$

The determinant of \mathbf{M} is equal to zero if the coefficient a_{32} or its cofactor is zero. Since the coefficient a_{32} is obtained from the boundary condition $\sigma_{r\theta} = 0$ at the Uranium/Sodium interface, and taking into account that if $n = 0$, then $u_r^1 = u_z^1 = 0$, expression (9) and the Hooke's law allow to get :

$$\sigma_{r\theta} = \mu_1 \left(r_1 \frac{\partial}{\partial r} \left(\frac{u_\theta^1}{r} \right) \right) = D_{11} \mu_1 \beta_1 \left(\frac{1}{r_1} Z_0'(\beta_1 r) - \beta_1 Z_0''(\beta_1 r) \right) = 0 \quad (17)$$

where $Z_n'' = \frac{\partial^2 Z_n}{\partial r^2}$. Hence, we have

$$a_{32} = Z_0'(\beta_1 r_1) - \beta_1 r_1 Z_0''(\beta_1 r_1) = 0 \quad (18)$$

From the Bessel differential equation, we get

$$Z_0''(\beta_1 r_1) = \left(\frac{n^2}{(\beta_1 r_1)^2} - 1 \right) Z_0(\beta_1 r_1) - \frac{1}{\beta_1 r_1} Z_0'(\beta_1 r_1).$$

Since $Z_0'(\beta_1 r_1) = -Z_1(\beta_1 r_1)$, we finally obtain:

$$\begin{aligned} Z_0'(\beta_1 r_1) - \beta_1 r_1 Z_0''(\beta_1 r_1) &= 0 \\ \iff (\beta_1 r_1) Z_0(\beta_1 r_1) &= 2 Z_1(\beta_1 r_1) \end{aligned} \quad (19)$$

This equation has an infinite number of solutions given by the zeros of the Bessel function of order 2. However, it does not account for the semi-infinite length of the Uranium core. Zemanek [13] and Mason ([12], p.141-149) have studied the impact of a semi-infinite length of the cylinder on Eq.(19). They have concluded that it would imply a strong energy focusing and cause large amplitude displacement, for particular frequencies, near the end section. This phenomenon, called "end resonance", allows to simplify Eq.(19) as follows :

$$(\beta_1 r_1) Z_0(\beta_1 r_1) = Z_1(\beta_1 r_1). \quad (20)$$

Knowing the S -wave velocity in Uranium, the frequency associated with the first root of Eq.(20) is then given by [16]:

$$f_0 = \frac{1.841 c_s \sqrt{2}}{2\pi r_1} = \frac{1.841 \times 2020 \times \sqrt{2}}{2 \times 0.00475\pi} = 176.22 \text{ kHz} \quad (21)$$

This value suggests that the strongly energetic frequency, observed before the beginning of most of RIA (cf Figure 1), is a resonant frequency of the test device. This might not be associated with any environmental noise.

IV. NUMERICAL MODELING OF WAVE PROPAGATION IN THE SIMPLIFIED TEST DEVICE

We used a spectral-element method (SEM) for the numerical modeling of wave propagation in the test device. The goal is to evaluate the transfer function h_1 of the structure and the impact of the location of both the source and the receiver on the recorded signals. The influence of the type of the heat transfer fluid is also investigated (Water or Sodium). Hereafter, we consider the simplified test device represented in Figure 4a.

A. Brief recall on the spectral-element method

Since a couple of decades the SEM, which is a full-wave method initially introduced in fluid mechanics, has been successfully applied for wave propagation and imaging issues, more particularly in geophysics [17], in underwater acoustics [18] and in non-destructive testing [19]. This method is based upon a high-order piecewise polynomial approximation of the weak formulation of the wave equation. It combines the accuracy of the pseudospectral method with the flexibility of the finite-element method. In the SEM, the wavefield is represented in terms of high-degree Lagrange interpolants, and integrals are computed based upon Gauss-Lobatto-Legendre (GLL) quadrature. This combination leading to a perfectly diagonal mass matrix leads in turn to a fully explicit time scheme which lends itself very well to numerical simulations on parallel computers. It is particularly well suited to handling complex geometries and interface matching conditions [18]. As for each finite-element method, the SEM requires a meshing of the studied domain, but the standard GLL quadrature requires a quadrangular mesh in $2D$ or a hexaedral mesh in $3D$. For further details, the reader can refer, for instance, to [20].

B. Implementation of the spectral-element method

1) *Meshing*: Since the simplified test device can be considered as a cylinder with a symmetry axis along the Oz axis, we performed the numerical simulations in a $2D$ axisymmetric configuration. For the location of the source along the Oz axis, the $2D$ axi-symmetrical simulations are then equivalent to $3D$ simulations. We thus meshed the simplified test device in $2D$ with quadrangles using the open-source software package GMSH [21].

Since we use a high-order finite element method (namely, a 5^{th} -order method), the typical element size which is required to generate a correct mesh is of the order of the smallest wavelength λ_m travelling in the model. This wavelength is associated to the smallest wave velocity and the highest frequency. For the simplified test device, the smallest wave velocity is that of the P waves in the heat transfer fluid ($2300m/s$ for Sodium and $1436 m/s$ for Water), and the expected highest frequency of the signals should be around $200kHz$. As a

consequence, the smallest element size should be smaller than $\lambda_m = 7mm$ ($11mm$, respectively) for Water (for Sodium, respectively). However, considering the (small) thickness of the material layers of the test device, we chose $\lambda_m = 1mm$.

2) *Numerical computations*: We used the $2D$ axisymmetric version of the open-source software SPECSEM which implements the spectral-element method [22]. The source is a point source with a Dirac-like behavior in time. Its spectral response is flat within a very wide frequency band which is much greater than the maximum frequency considered here. Since SPECSEM is a time-domain numerical code, we need to use a time scheme for the computation of the solution. Here, we used a Newmark scheme for time-marching. In addition to an adequate spatial sampling, it is also necessary to have an adequate time sampling which ensures the stability of the numerical simulations. The value of the time interval dt is driven by the well-known Courant-Friedrichs-Lewy (CFL) condition. For a Newmark scheme, the CFL number must be less than 0.5. As a consequence, we chose $dt = 2 \cdot 10^{-9}$, which gives a CFL number equal to 0.3, and hence ensures the stability of our numerical simulations.

C. Results

1) *Resonant frequency of the test device*: Firstly, the transfer function of the test device was computed numerically for the case of a point source located on the fuel clad, the receiver being located at the position of the sensor 2 ($M2$) (cf. Figure 2). Its normalized spectrum clearly highlights, with a small shift towards the high frequencies, the strongly energetic component around $180kHz$ (Figure 5), already observed in the normalized spectrum of the environmental noise and confirmed by the analytical derivations. Therefore, it is confirmed that this acoustic component is a resonant frequency of the test device.

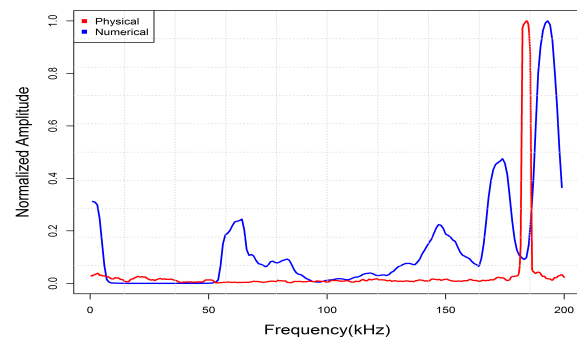


Figure 5: Superposition of the normalized spectrum associated with the environmental noise (red) and the normalized spectrum of the transfer function of the simplified test device (blue), for the case of a point source located on the fuel clad.

2) *Influence of the location of both the source and the receiver on the transfer function of the test device*: Secondly, we simulated the recorded signals associated with various

source/receiver pairs, in order to analyze the impact of a change in the source (receiver, respectively) location on these signals, and hence on the transfer function of the test device. More specifically, Figure 6 illustrates the impact of the source location (inside the fuel, on the fuel clad, and inside the Sodium layer, respectively) on the spectrum of the transfer function, the receiver located at the position of the sensor 1 ($M1$) being fixed. For a given source, the impact of the receiver location can be observed in Figure 7.

We can clearly see that no global transfer function of the test device can be defined from these results. Indeed, the associated spectrum has very different spectral contents depending on the location of the source/receiver pair. In particular, for a given receiver, moving the source from a location in one device layer to a location in another layer involves enhancing or neglecting specific propagation phenomena, which leads to the modification of the frequency matrix, and hence the emergence of various energetic frequencies in the transfer function spectrum (Figure 6). Moreover, both the receiver location and the coupling to the test device have significant effect on the recorded signal characteristics (Figure 7). Consequently, if the location of the source mechanism is *a priori* unknown, classical deconvolution methods are not convenient to remove the impact of the test device from the recorded signals.

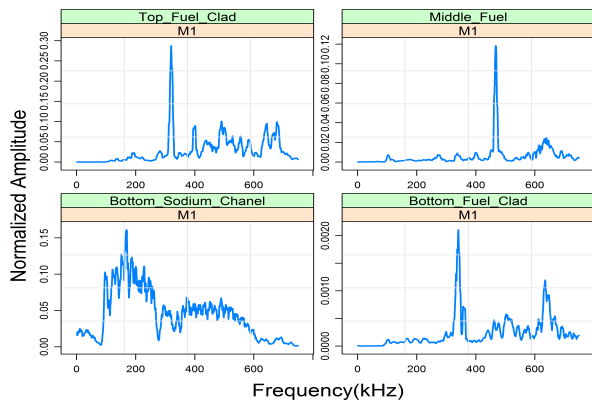


Figure 6: Impact of a change in the source location on the spectrum of the transfer function of the test device, the receiver located at $M1$ being fixed.

3) *Analysis of the transfer function according to various frequency ranges:* Now consider the transfer functions associated with various source locations on the fuel clad and with various receiver locations ($M1$ or $M2$). Locating the source on the fuel clad is of great interest, since physical mechanisms of major importance such as clad failures may occur there during a RIA. Analysis of the transfer function spectra in the frequency range $[0, 200]$ kHz shows two interesting results (Figure 8). On one hand, the spectral component around 180 kHz is still observed, whatever the receiver location. On the other hand, since the spectra are quasi constant up to 50 kHz, there is no significant impact of the test device on the recorded signals within this frequency range. Therefore, we expect that the spectral components of the signals generated by source mechanisms located on the fuel clad (for instance,

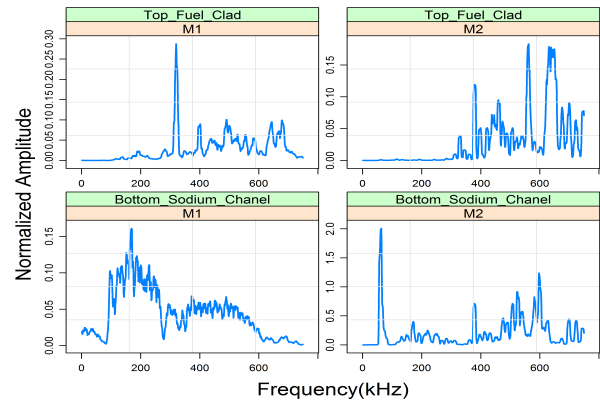


Figure 7: Impact of a change in the receiver location on the spectrum of the transfer function of the test device, the source being fixed.

clad failures), and recorded by the receivers whose resonant frequency is around 25 kHz, may not be affected by the test device.

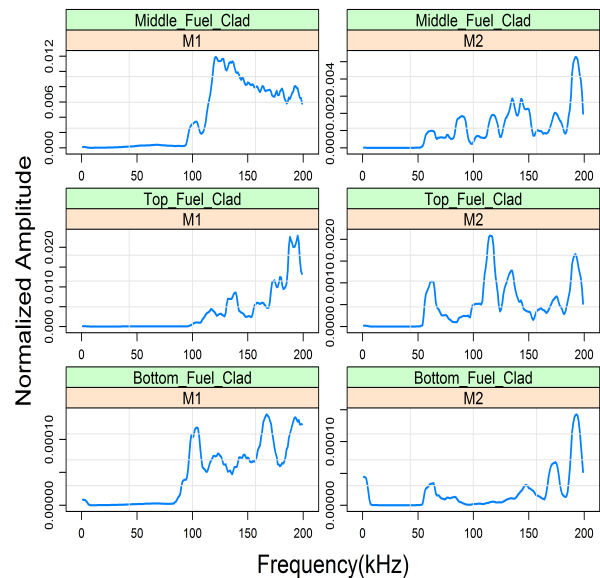


Figure 8: Focus, within the frequency range $[0, 200]$ kHz, on the transfer function spectra for various source locations on the fuel clad and for the two receivers (located at $M1$ and $M2$).

4) *Impact of the heat transfer fluid:* In order to evaluate the impact of a change in the heat transfer fluid on wave propagation, we analyze the pressure distribution inside the test device at different times, when the source is located at the center of the fuel layer. Figure 9 is focused more specifically on the domain of Figure 4a which is composed of three zones, namely, a part of the Stainless steel support and a part of the fuel (Uranium)/clad (Zircaloy) domain (Zone 1), the heat transfer fluid (Zone 2), and the outer layer of Zircaloy (Zone 3).

Whatever the kind of the heat transfer fluid (Water or liquid

Sodium), three main zones of acoustical activity can be distinguished.

Within Zone 1 (where the source is located), the normal stress distribution seems to be independent on the kind of the heat transfer fluid. This observation is in agreement with the high impedance contrast between media of Zones 1 and 2 (see Table I). Furthermore, no significant discontinuity between the Stainless steel support and the fuel (Uranium)/clad (Zircaloy) domain is observed, which thus confirms the relevance of our assumptions likening these two regions to a single homogeneous region equivalent to Uranium in the analytical derivations.

Within Zone 2, the effect of the heat transfer fluid is significant, in particular for short times (see snapshots at $t = 36\mu s$ in Figure 9) for which the transmitted wavefronts at the interfaces between Zones 1 – 2 and 2 – 3 are logically faster and more developed for the case of Sodium. For longer times (see snapshots at $t = 100\mu s$ in Figure 9) for which the modal propagation regime is well established in Zones 2 and 3, we still observe quite similar patterns whatever the heat transfer fluid, however, with greater spatial wavelengths for the case of Sodium. By examining more carefully the signals recorded at the receiver, and more specifically their spectrum (Figure 10), we can note that replacing Water by Sodium leads to an increase in the recorded signal amplitude and a small shift of the frequency content towards the high frequencies.

V. CONCLUSION

The main goal of this paper was twofold : identifying the source of the strongly energetic spectral component around $180kHz$, observed in the operating noise of the nuclear reactor before the beginning of RIA, and evaluating the impact of wave travelpath in the test device on the AE signals recorded during RIA experiments. In order to understand wave propagation, two complementary approaches have then been applied. First, based on geometrical and acoustical simplifications of the complex test device, analytical derivations of torsional wave propagation have highlighted a resonant frequency around $180kHz$ which is consistent with experimental observations. In a second step, from numerical simulations of wave propagation based on a spectral-element method, the transfer function of the test device has been shown to be strongly dependent on both the source and the receiver locations, which precludes signal processing by deconvolution when the location of the AE source mechanism is unknown. However, filtering or penalizing the recorded signal components which are associated with the frequency range around $180kHz$ may be appropriate. The numerical results also suggest that the geometry and the configuration of the test device do not influence the source signal characteristics up to $50kHz$. Therefore, the spectral components of the signals generated by source mechanisms located on the fuel clad (for instance, clad failures) may not be affected by the test device. Finally, replacing the heat transfer (Water) fluid by liquid Sodium leads to an increase in the recorded signal amplitude and a small shift of the frequency content towards the high frequencies. The results obtained in this paper may be useful,

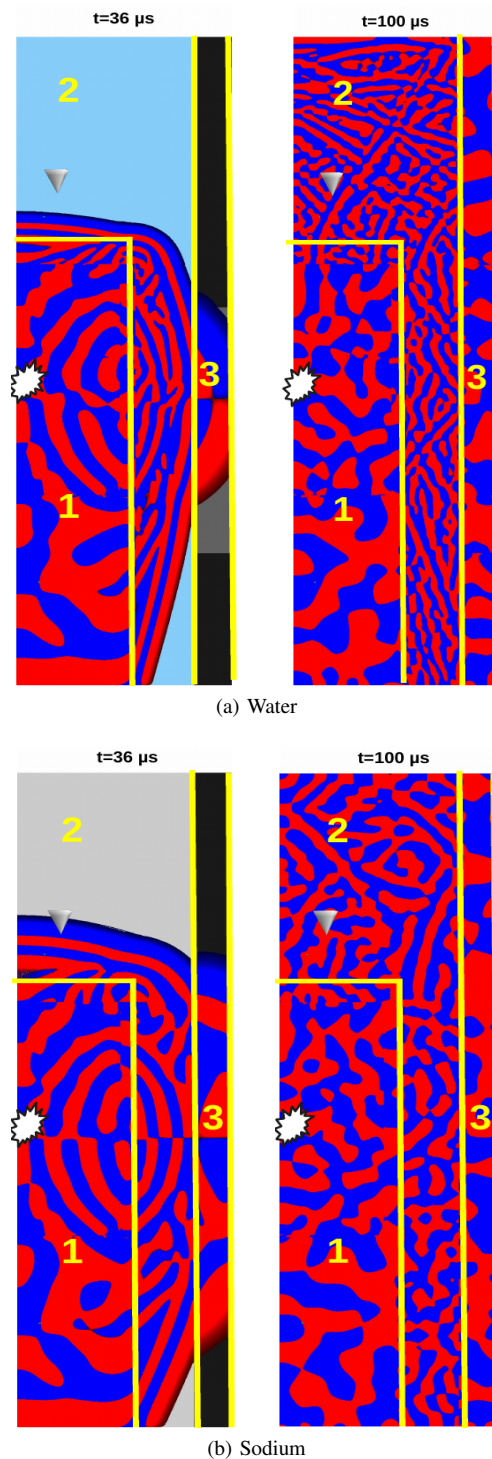


Figure 9: Snapshots (at different times) of the normal stress/pressure distribution in the core of the test device for two kinds of heat transfer fluid. Zone 1 corresponds to a part of the Stainless steel support and a part of the fuel (Uranium)/clad (Zircaloy) domain, whereas Zones 2 and 3 correspond to the heat transfer fluid and the outer layer of Zircaloy, respectively. The source location is denoted by a white star, and the receiver location by a grey triangle.

for instance, to improve design of future RIA experiments.

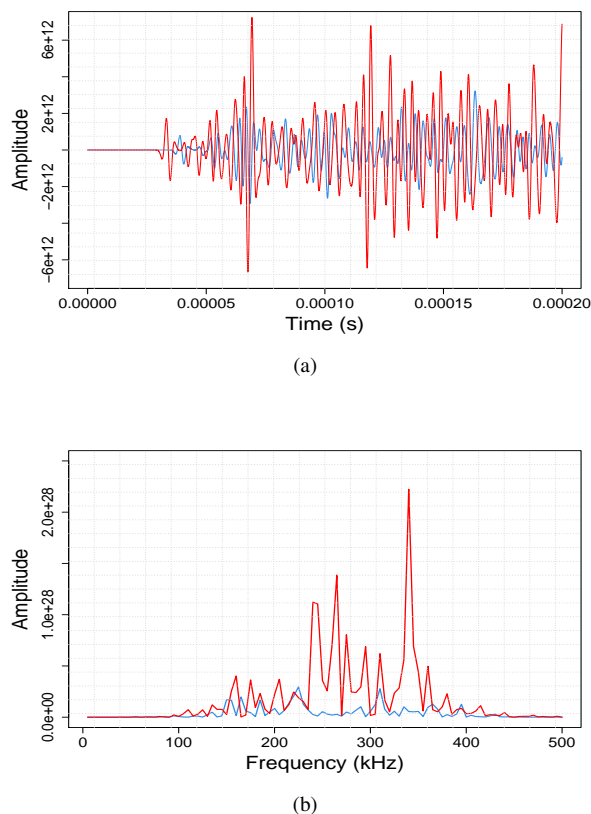


Figure 10: Simulated signals (a) and associated spectra (b) obtained when the source is located inside the fuel (cf. Figure 9) and the receiver in the Water (blue) or Sodium (red) fluid.

They are undoubtedly useful to understand wave propagation in the core of the nuclear reactor, and to choose appropriate signal processing tools for recovering the source of AE signals generated during RIA experiments.

Another perspective to this work would be to perform measurements of acoustic wave propagation in realistic mock-ups of the test device. The obtained signals would then constitute valuable datasets for the validation of the numerical results, but also for the optimization of the location of the two sensors in order to decrease as much as possible the strong impact of this location on the transfer function of the test device.

ACKNOWLEDGMENT

The authors thank the reviewers for relevant suggestions which have improved the paper.

This work was granted access to the HPC resources of Aix-Marseille Université financed by the project Equip@Meso (ANR-10-EQPX-29-01) of the program « Investissements d'Avenir » supervised by the Agence Nationale de la Recherche.

REFERENCES

[1] Q. Ai, C. Liu, X. Chen, P. He, and Y. Wang. Acoustic emission of fatigue crack in pressure pipe under cyclic pressure. *Nuclear Engineering and Design*, 240(10):3616–3620, 2010.

[2] D. S. Kupperman, T. N. Claytor, and R. Groenwald. Acoustic leak detection for reactor coolant systems. *Nuclear Engineering and Design*, 86(1):13–20, 1985.

[3] C. B. Scruby and H. N. Wadley. An assessment of acoustic emission for nuclear pressure vessel monitoring. *Progress in Nuclear Energy*, 11(3):275–297, 1983.

[4] L. Hégron, P. Sornay, and N. Favretto-Cristini. Compaction of a bed of fragmentable particles and associated acoustic emission. *IEEE Transactions on Nuclear Science*, 61(4):2175–2181, 2014.

[5] N. Favretto-Cristini, L. Hégron, and P. Sornay. Identification of the fragmentation of brittle particles during compaction process by the acoustic emission technique. *Ultrasonics*, 67:178–189, 2016.

[6] G. Gauschi. *Piezoelectric sensors: force, strain, pressure, acceleration and acoustic emission sensors, materials and amplifiers*. Springer Science & Business Media, 2002.

[7] V. Barat, Y. Borodin, and A. Kuzmin. Intelligent acoustic emission signal filtering methods. *Journal of Acoustic Emission*, 28:109–119, 2010.

[8] O.I. Traore, L. Pantera, N. Favretto-Cristini, P. Cristini, S. Viguier-Pla, and P. Vieu. Structure analysis and denoising using singular spectrum analysis: application to acoustic emission signals from nuclear safety experiments. *Measurement*, 104:78 – 88, 2017.

[9] C. U. Grosse and M. Ohtsu. *Acoustic emission testing*. Springer Science & Business Media, 2008.

[10] T. Le Gall. *Simulation of acoustic emission : Assisting in identification of acoustic signature of damage mechanisms*. Phd thesis, Université de Lyon, January 2016.

[11] D.C. Gazis. Three-dimensional investigation of the propagation of waves in hollow circular cylinders. I. Analytical foundation. *The Journal of the Acoustical Society of America*, 31(5):568–573, 1959.

[12] W.P. Mason. *Physical Acoustics: Principles and Methods*, volume 1. Part A. Academic Press, 1971.

[13] J. Zemanek Jr. An experimental and theoretical investigation of elastic wave propagation in a cylinder. *The Journal of the Acoustical Society of America*, 51(1B):265–283, 1972.

[14] R.D. Doolittle and H. Überall. Sound scattering by elastic cylindrical shells. *The Journal of the Acoustical Society of America*, 39(2):272–275, 1966.

[15] D.C. Gazis. Exact analysis of the plane-strain vibrations of thick-walled hollow cylinders. *The Journal of the Acoustical Society of America*, 30(8):786–794, 1958.

[16] M. Onoe. *Tables of Modified Quotients of Bessel Functions of the First Kind for Real and Imaginary Arguments*. Columbia University Press, 1958.

[17] J. Tromp, D. Komatitsch, and Q. Liu. Spectral-element and adjoint methods in seismology. *Communications in Computational Physics*, 3(1):1–32, 2008.

[18] P. Cristini and D. Komatitsch. Some illustrative examples of the use of a spectral-element method in ocean acoustics. *The Journal of the Acoustical Society of America*, 131(3):EL229–EL235, 2012.

[19] D. Komatitsch, J.M. Carcione, F. Cavallini, and N. Favretto-Cristini. Elastic surface waves in crystals—Part 2: Cross-check of two full-wave numerical modeling methods. *Ultrasonics*, 51(8):878–889, 2011.

[20] A. Fichtner. *Full seismic waveform modelling and inversion*. Springer-Verlag, 2010.

[21] C. Geuzaine and J.F. Remacle. GMSH: A 3D finite element mesh generator with built-in pre-and post-processing facilities. *International Journal for Numerical Methods in Engineering*, 79(11):1309–1331, 2009.

[22] Alexis Bottero, Paul Cristini, Dimitri Komatitsch, and Mark Asch. An axisymmetric time-domain spectral-element method for full-wave simulations: Application to ocean acoustics. *The Journal of the Acoustical Society of America*, 140(5):3520–3530, 2016.

APPENDIX A

BOUNDARY CONDITIONS AT THE INTERFACES INSIDE THE TEST DEVICE

The generalized Hooke's law expresses the normal and tangential stresses σ_{rr} and $\sigma_{r\theta}$ as functions of the corresponding strains :

$$\sigma_{rr} = \lambda \Delta \phi + 2\mu \epsilon_{rr}, \quad \sigma_{r\theta} = 2\mu \epsilon_{r\theta} \quad (22)$$

where the strains can be written as a function of the displacements u_r and u_θ :

$$\epsilon_{rr} = \frac{\partial u_r}{\partial r}, \quad \epsilon_{r\theta} = \frac{1}{2} \left(r \frac{\partial}{\partial r} \left(\frac{u_\theta}{r} \right) + \frac{1}{r} \frac{\partial u_r}{\partial \theta} \right) \quad (23)$$

We thus obtain :

$$\begin{aligned} \sigma_{rr} = & [A_1 (-\lambda(\alpha^2 + k^2)Z_n(\alpha r) + 2\mu \alpha^2 Z_n''(\alpha r)) \\ & + A_2 (-\lambda(\alpha^2 + k^2)W_n(\alpha r) + 2\mu \alpha^2 W_n''(\alpha r)) \\ & + D_1 \left(\frac{n}{r} \alpha Z_n'(\beta r) - \frac{n}{r^2} Z_n(\beta r) \right) \\ & + D_2 \left(\frac{n}{r} \alpha W_n'(\beta r) - \frac{n}{r^2} W_n(\beta r) \right)] \cos(n\theta) \end{aligned} \quad (24)$$

$$\begin{aligned} \sigma_{r\theta} = & \left[A_1 \left[2n \mu \left(\frac{1}{r^2} Z_n(\alpha r) - Z_n'(\alpha r) \right) \right] \right. \\ & + A_2 \left[2n \mu \left(\frac{1}{r^2} W_n(\alpha r) - W_n'(\alpha r) \right) \right] \\ & + D_1 [\beta^2 (Z_n(\beta r) - 2Z_n''(\beta r))] \\ & \left. + D_2 [\beta^2 (W_n(\beta r) - 2W_n''(\beta r))] \right] \sin(n\theta) \end{aligned} \quad (25)$$

We recall that, for the case of the Uranium core, Eqs (25) and (26) can be simplified since $W_n = 0$ (cf. Eq. (9)).

The boundary conditions at the different interfaces inside the test device can then be easily derived.

a) Boundary conditions at the Uranium/Sodium interface: We first recall that the index of the Uranium core is denoted by 1, whereas that of the heat transfer fluid (Sodium) is 2. Knowing that the pressure in Sodium is linked to the scalar potential through $p = \rho_2 \frac{\partial^2 \phi_2}{\partial t^2}$, the boundary conditions (Eq. (13)) can be expressed by :

$$\begin{aligned} A_{11} (-\lambda_1(\alpha_1^2 + k_1^2)Z_n(\alpha_1 r_1) + 2\mu_1 \alpha_1^2 Z_n''(\alpha_1 r_1)) \\ + D_{11} \left(\frac{n}{r_1} \alpha_1 Z_n'(\beta_1 r_1) - \frac{n}{r_1^2} Z_n(\beta_1 r_1) \right) \\ + E_{21} (\rho_2 \omega Z_n(\alpha_2 r_1)) + E_{22} (\rho_2 \omega W_n(\alpha_2 r_1)) = 0 \end{aligned} \quad (26)$$

$$\begin{aligned} A_{11} \alpha_1 Z_n'(\alpha_1 r_1) + D_{11} \frac{n}{r_1} Z_n(\beta_1 r_1) \\ + E_{21} \alpha_2 Z_n'(\alpha_2 r_1) + E_{22} \alpha_2 W_n'(\alpha_2 r_1) = 0 \end{aligned} \quad (27)$$

$$\begin{aligned} A_{11} 2n \mu_1 \left(\frac{1}{r_1^2} Z_n(\alpha_1 r) - Z_n'(\alpha_1 r_1) \right) \\ + D_{11} \beta_1^2 (Z_n(\beta_1 r_1) - 2Z_n''(\beta_1 r_1)) = 0 \end{aligned} \quad (28)$$

b) Boundary conditions at the Sodium/Zircaloy interface:

The index of the outer layer (Zircaloy) being denoted by 3, the boundary conditions (Eq. (13)) can be written as :

$$\begin{aligned} E_{21} \rho_2 \omega Z_n(\alpha_2 r_2) + E_{22} \rho_2 \omega W_n(\alpha_2 r_2) \\ + A_{31} (-\lambda_3(\alpha_3^2 + k_3^2)Z_n(\alpha_3 r_2) + 2\mu_3 \alpha_3^2 Z_n''(\alpha_3 r_2)) \\ + A_{32} (-\lambda_3(\alpha_3^2 + k_3^2)W_n(\alpha_3 r_2) + 2\mu_3 \alpha_3^2 W_n''(\alpha_3 r_2)) \\ + D_{31} \left(\frac{n}{r_2} \alpha_3 Z_n'(\beta_3 r_2) - \frac{n}{r_2^2} Z_n(\beta_3 r_2) \right) \\ + D_{32} \left(\frac{n}{r_2} \alpha_3 W_n'(\beta_3 r_2) - \frac{n}{r_2^2} W_n(\beta_3 r_2) \right) = 0 \end{aligned} \quad (29)$$

$$\begin{aligned} E_{21} \alpha_2 Z_n'(\alpha_2 r_2) + E_{22} \alpha_2 W_n'(\alpha_2 r_2) \\ + A_{31} \alpha_3 Z_n'(\alpha_3 r_2) + A_{32} \alpha_3 W_n'(\alpha_3 r_2) \\ + D_{31} \frac{n}{r_2} Z_n(\beta_3 r_2) + D_{32} \frac{n}{r_2} W_n(\beta_3 r_2) = 0 \end{aligned} \quad (30)$$

$$\begin{aligned} A_{31} 2n \mu_3 \left(\frac{1}{r_2^2} Z_n(\alpha_3 r_2) - Z_n'(\alpha_3 r_2) \right) \\ + A_{32} 2n \mu_3 \left(\frac{1}{r_2^2} W_n(\alpha_3 r_2) - W_n'(\alpha_3 r_2) \right) \\ + D_{31} \beta_3^2 (Z_n(\beta_3 r_2) - 2Z_n''(\beta_3 r_2)) \\ + D_{32} \beta_3^2 (W_n(\beta_3 r_2) - 2W_n''(\beta_3 r_2)) = 0 \end{aligned} \quad (31)$$

c) Free surface condition at the surface of the Zircaloy layer: The free surface condition (Eq. (14)) implies :

$$\begin{aligned} A_{31} (-\lambda_3(\alpha_3^2 + k_3^2)Z_n(\alpha_3 r_3) + 2\mu_3 \alpha_3^2 Z_n''(\alpha_3 r_3)) \\ + A_{32} (-\lambda_3(\alpha_3^2 + k_3^2)W_n(\alpha_3 r_3) + 2\mu_3 \alpha_3^2 W_n''(\alpha_3 r_3)) \\ + D_{31} \left(\frac{n}{r_3} \alpha_3 Z_n'(\beta_3 r_3) - \frac{n}{r_3^2} Z_n(\beta_3 r_3) \right) \\ + D_{32} \left(\frac{n}{r_3} \alpha_3 W_n'(\beta_3 r_3) - \frac{n}{r_3^2} W_n(\beta_3 r_3) \right) = 0 \end{aligned} \quad (32)$$

$$\begin{aligned} A_{31} 2n \mu_3 \left(\frac{1}{r_3^2} Z_n(\alpha_3 r_3) - Z_n'(\alpha_3 r_3) \right) \\ + A_{32} 2n \mu_3 \left(\frac{1}{r_3^2} W_n(\alpha_3 r_3) - W_n'(\alpha_3 r_3) \right) \\ + D_{31} \beta_3^2 (Z_n(\beta_3 r_3) - 2Z_n''(\beta_3 r_3)) \\ + D_{32} \beta_3^2 (W_n(\beta_3 r_3) - 2W_n''(\beta_3 r_3)) = 0 \end{aligned} \quad (33)$$

APPENDIX B

COEFFICIENTS OF THE FREQUENCY MATRIX

$$\begin{aligned} a_{11} &= -\lambda_1(\alpha_1^2 + k_1^2)Z_n(\alpha_1 r_1) + 2\mu_1 \alpha_1^2 Z_n''(\alpha_1 r_1) \\ a_{12} &= \frac{n}{r_1} \alpha_1 Z_n'(\beta_1 r_1) - \frac{n}{r_1^2} Z_n(\beta_1 r_1) \\ a_{13} &= \rho_2 \omega Z_n(\alpha_2 r_1) \\ a_{14} &= \rho_2 \omega W_n(\alpha_2 r_1) \\ a_{15} &= a_{16} = a_{17} = a_{18} = 0 \\ a_{21} &= \alpha_1 Z_n'(\alpha_1 r_1) \\ a_{22} &= \frac{n}{r_1} Z_n(\beta_1 r_1) \\ a_{23} &= \alpha_2 Z_n'(\alpha_2 r_1) \\ a_{24} &= \alpha_2 W_n'(\alpha_2 r_1) \\ a_{25} &= a_{26} = a_{27} = a_{28} = 0 \\ a_{31} &= 2n \mu_1 \left(\frac{1}{r_1^2} Z_n(\alpha_1 r) - Z_n'(\alpha_1 r_1) \right) \\ a_{32} &= \beta_1^2 (Z_n(\beta_1 r_1) - 2Z_n''(\beta_1 r_1)) \\ a_{33} &= a_{34} = a_{35} = a_{36} = a_{37} = a_{38} = 0 \\ a_{41} &= a_{42} = 0 \\ a_{43} &= \rho_2 \omega Z_n(\alpha_2 r_2) \\ a_{44} &= \rho_2 \omega W_n(\alpha_2 r_2) \\ a_{45} &= -\lambda_3(\alpha_3^2 + k_3^2)Z_n(\alpha_3 r_2) + 2\mu_3 \alpha_3^2 Z_n''(\alpha_3 r_2) \\ a_{46} &= -\lambda_3(\alpha_3^2 + k_3^2)W_n(\alpha_3 r_2) + 2\mu_3 \alpha_3^2 W_n''(\alpha_3 r_2) \\ a_{47} &= \frac{n}{r_2} \alpha_3 Z_n'(\beta_3 r_2) - \frac{n}{r_2^2} Z_n(\beta_3 r_2) \\ a_{48} &= \frac{n}{r_2} \alpha_3 W_n'(\beta_3 r_2) - \frac{n}{r_2^2} W_n(\beta_3 r_2) \end{aligned}$$

$$\begin{aligned}
a_{51} &= a_{52} = 0 \\
a_{53} &= \alpha_2 Z'_n(\alpha_2 r_2) \\
a_{54} &= \alpha_2 W'_n(\alpha_2 r_2) \\
a_{55} &= \alpha_3 Z'_n(\alpha_3 r_2) \\
a_{56} &= \alpha_3 W'_n(\alpha_3 r_2) \\
a_{57} &= \frac{n}{r} Z_n(\beta_3 r_2) \\
a_{58} &= \frac{n}{r} W_n(\beta_3 r_2) \\
a_{61} &= a_{62} = a_{63} = a_{64} = 0 \\
a_{65} &= 2n \mu_3 \left(\frac{1}{r_2^2} Z_n(\alpha_3 r_2) - Z'_n(\alpha_3 r_2) \right) \\
a_{66} &= 2n \mu_3 \left(\frac{1}{r_2^2} W_n(\alpha_3 r_2) - W'_n(\alpha_3 r_2) \right) \\
a_{67} &= \beta_3^2 (Z_n(\beta_3 r_2) - 2Z''_n(\beta_3 r_2)) \\
a_{68} &= \beta_3^2 (W_n(\beta_3 r_2) - 2W''_n(\beta_3 r_2)) \\
a_{71} &= a_{72} = a_{73} = a_{74} = 0 \\
a_{75} &= (-\lambda_3(\alpha_3^2 + k_3^2)Z_n(\alpha_3 r_3) + 2\mu_3 \alpha_3^2 Z''_n(\alpha_3 r_3)) \\
a_{76} &= (-\lambda_3(\alpha_3^2 + k_3^2)W_n(\alpha_3 r_3) + 2\mu_3 \alpha_3^2 W''_n(\alpha_3 r_3)) \\
a_{77} &= \left(\frac{n}{r_3} \alpha_3 Z'_n(\beta_3 r_3) - \frac{n}{r_3} Z_n(\beta_3 r_3) \right) \\
a_{78} &= \left(\frac{n}{r_3} \alpha_3 W'_n(\beta_3 r_3) - \frac{n}{r_3} W_n(\beta_3 r_3) \right) \\
a_{81} &= a_{82} = a_{83} = a_{84} = 0 \\
a_{85} &= 2n \mu_3 \left(\frac{1}{r_3^2} Z_n(\alpha_3 r_3) - Z'_n(\alpha_3 r_3) \right) \\
a_{86} &= 2n \mu_3 \left(\frac{1}{r_3^2} W_n(\alpha_3 r_3) - W'_n(\alpha_3 r_3) \right) \\
a_{87} &= \beta_3^2 (Z_n(\beta_3 r_3) - 2Z''_n(\beta_3 r_3)) \\
a_{88} &= \beta_3^2 (W_n(\beta_3 r_3) - 2W''_n(\beta_3 r_3))
\end{aligned}$$